Geotechnical Engineering Journal of the SEAGS & AGSSEA Vol. 45 No.4 December 2014 ISSN 0046-5828

Eulerian–Lagrangian Modeling of Current-Induced Coastal Sand Dune Migration

R. Sun[1] and H. Xiao[2*]

[1]*Department of Aerospace and Ocean Engineering, Virginia Tech, Blacksburg, Virginia, USA*

[2*]*E-mail*: hengxiao@vt.edu

ABSTRACT: In this work, an Eulerian–Lagrangian framework is developed for the modeling of current-induced sediment transport and sand dune migration. In this framework, the fluid flow is modeled by solving the Reynolds-averaged Navier–Stokes (RANS) equations, and a conservation equation is used to describe the morphological evolution of the sand bed, both of which are formulated in the Eulerian framework. Empirical models are used for the erosion, the dispersion, and the drag and lift forces exerted on the sediment particles. The trajectories of individual particles are tracked in the Lagrangian framework, which enables a high-fidelity representation of the particle motions and composition statistics, as well as direct representation of sediment deposition without the need of ad hoc models. This framework consists of four tightly coupled modules: (1) a fluid flow solver based on RANS equations, (2) a morphological evolution modeling equation, (3) a Lagrangian particle-tracking scheme for suspended sediments, and (4) a dynamic mesh motion solver which deforms the mesh to account for the effects of morphological evolution on the flow field. The developed framework is validated by using previous results in the literature and is used to simulate coastal sand dune formation migration. Favorable agreements with benchmark results are obtained, demonstrating potential of the developed Eulerian–Lagrangian modeling framework for sediment transport.

KEYWORDS: Sediment transport, Fluid–particle interaction, Computational fluid dynamics, Sand dune migration

1. INTRODUCTION

The interaction between hydrodynamics and morphological evolution of the seabed plays an important role in the coastal region. The understanding of current-induced morphological evolution of seabed is critical for the study of large-scale sediment transport processes and for the effective utilization of coastal resources including marine renewable energy harvesting as well as oil and gas extraction. For example, the installation and operation of wave energy converters and tidal turbines have to take account of the geotechnical conditions of the seabed and the sediment concentration in the proposed region of development, and the influences of deposited sediments to the devices needs to be assessed (e.g., Neil et al. 2009; Willis et al. 2010); scour around piles must be studied to ensure the safety of the offshore structures (e.g., Rouland et al. 2005). Therefore, understanding the sediment transport processes and the associated morphological evolution is critical for the design, construction, and safety assessment of coastal structures and installations. However, the morphological evolution of the seabed and the hydrodynamics of the currents are highly coupled nonlinear processes. Specifically, morphological evolution of the seabed leads to modified boundaries for the flow, which cause changes in the flow field; the changed flow field in turn reshapes the seabed via erosion and deposition. Consequently, accurate simulation and modeling of these processes poses significant challenge.

Current-induced migration of sand dunes is a critical phenomenon in coastal regions. Understanding the physics of these processes serves as the baseline for investigating scour and sediment transport around coastal structures. The flow over fixed dunes has been experimentally studied by many researchers to investigate the flow field quantities including velocity, wall shear stress, and turbulent kinetic energy. Mierlo and Ruiter (1988) measured the turbulent flow over stationary, artificial dunes, and obtained instantaneous velocity and pressure fields of the flow. Hudson et al. (1996) performed experiments over a sinusoidal wavy bed as opposed to the dune-shaped bed geometry in the measurement of Mierlo and Ruiter (1988). They studied the turbulence flow characteristics by investigating the fluctuations of velocities and turbulent shear stresses. Another experimental study of flow over low-angle dune model conducted by Best et al. (2002) showed that the morphology of a dune had major influences on the turbulence of the flow.

Instead of focusing on the features of the flow over a fixed dune, some authors studied the dune migration induced by the flow. Coleman et al. (1994) measured the formation of bed form features starting from a flat bed. They investigated the relationship between the speed of dune migration and the dune height through a series of 47 experiments. Venditti and Church (2005) studied the influence of dune angles to the migration rates by comparing the kinematics and morphodynamics of low-angle and high-angle sand dunes. These experiments provide extensive physical insights to the flow over sand dunes and the migration of sand dunes due to the flow. However, all the above-mentioned studies are laboratory-scale experiments. Due to the various physical processes and non-dimensional numbers involved, it is not possible to preserve all important non-dimensional numbers. This may prevent many field-scale physics to be properly represented in the laboratory-scale experiments. Field-scale sediment transport experiments and observations are, however, very expensive to conduct, and precise control of experimental conditions is difficult.

Numerical models offer an attractive alternative for experimental sediment transport studies, and they have been used to study sand dune migration by many authors in the past few decades. Nelson et al. (1989) studied the mechanics of flow over fixed dunes and developed an empirical model for the prediction of velocity and boundary shear stress over two-dimensional dunes. Although the comparison of their model predictions with the experimental results was favourable, their model requires several input parameters that are difficult to obtain for different dune shapes. Yoon et al. (1996) studied the flow over the same fixed sand dune as in the experiments of Nelson et al. (1989) by using Reynolds-Averaged Navier–Stokes (RANS) simulations. Cherukat et al. (1998) studied the fully developed turbulent flow over a sinusoidal wavy surface using Direct Numerical Simulations (DNS) and compared their results with experimental data (e.g., Hudson et al. (1996)). Chang and Scotti (2004) studied the turbulent flow in the same geometry as Cherukat et al. (1998) and compared results obtained from RANS simulations and Large Eddy Simulations (LES). The conclusion of their study was that LES gave more accurate prediction than RANS did for flows of this geometry. However, since LES and DNS are both computationally expensive, and they have been mostly constrained to flows at relatively low Reynolds numbers (e.g., Cherukat et al. 1998; Chang and Scotti 2004). Applications of LES and DNS to field-scale problems are not yet feasible given today's computational resources. For problems of these scales, RANS will likely be the only affordable methodology in the decades to come. Knotek et al. (2014) solved RANS equations to obtain the shear stresses on a wavy boundary and developed an algebraic model for the prediction of shear stresses in various configurations. These simulations provided valuable data for the study of dune migration, and the comparison of different modeling approaches provided important knowledge in the performance of various numerical models in sand dune migration modeling. However, the simulations mentioned above used fixed sand dune and thus ignored the influence of the sediment transport and morphological modeling.

On the other hand, several other authors performed simulations using movable seabed with sediment transport accounted for. Giri et al. (2006) performed numerical simulations of sand dune migration in free surface flows based on RANS equations and compared with experimental results. Their numerical simulations agreed well with experimental data. Niemann et al. (2011) simulated the dune migration in a channel flow without free surface and obtained solution of dune profiles in equilibrium, which is consistent with experimental observations reported in the literature (e.g. Coleman et al. 1994; Kraft et al. 2011) used LES to study the turbulence in a channel and applied level set method to capture the interface between the sand dune and the turbulence flow. The migration of their simulation agreed well with experimental results. The transport of suspended sediments was obtained by solving a convection–diffusion equation for the concentration. Consequently, information of particle trajectory, velocity, and size distribution was not available due to the intrinsic limitation of the model based on the concentration equation. The particle trajectory information is important in identifying fundamental mechanisms of sediment transport. Moreover, with the concentration-based model for suspended sediments, ad hoc models are required for sediment dispersion and deposition, which introduces additional modeling uncertainties. This difficulty can be partly alleviated by using Lagrangian description of suspended sediment motions.

Tracking particle motion in the Lagrangian framework is a relatively new approach for the study of sediment transport in turbulent flow. Chang and Scotti (2003) studied the motion of particles in a channel with wavy boundary using LES. In their work, the fluid flow was not influenced by the presence of the particles. The particles are distributed uniformly on the boundary at start without using any erosion function and do no interact with the boundary. Escauriaza et al. (2011) developed a one-way coupled Eulerian–Lagrangian model to study the motion of particles in turbulent flow using detached eddy simulation and investigated the velocity and trajectory of the particles around the bridge pile. The ejection of particles was captured and the sediment flux was analysed statistically. However, the sediment grains were initially located in front of the cylinder, and no erosion or deposition of particles was considered in this work. Nabi and co-workers (e.g., Nabi et al. 2013a; Nabi et al. 2013b) performed simulations of the morphological change of three-dimensional underwater dunes using a Lagrangian framework to evaluate the suspension and deposition of particles. In their work, the process of dune migration was successfully simulated. Length and height of the developed dunes were compared with experimental measurements (e.g., Bakker et al. 1986; Crosato et al. 2011). However, the discrete-element modeling of the pickup and deposition in their work has high computational costs due to the large number of particles in typical sediment transport simulations, which severely limits the size of the system they can simulate.

Due to the limitations of existing models and the associated uncertainties in the modeling of sand dune migration processes, the objective of the present work is to develop and validate an Eulerian–Lagrangian framework for the study of the current-induced migration of coastal sand dunes. To validate this Eulerian–Lagrangian framework, numerical simulations of sand dune formation and migration processes are performed, and the simulation results are compared with the existing numerical simulations and experimental data in the literature. The rest of the paper is organized as follows. Section 2 presents the modeling framework used in this study, including the models for the fluid flow, the morphological evolution, and the transport of suspended particles, as well as the coupling between these modules. The numerical implementation of the framework in OpenFOAM is briefly discussed in Section 3. The developed framework is used to simulate current-induced dune migration, and the results are presented in Section 4. Finally, Section 5 concludes the paper.

2. MODELING METHODOLOGY

In the present work, we develop an Eulerian–Lagrangian framework to model the coupled flow and sediment transport processes, and this framework is used to simulate current-induced coastal sand dune migration. The Eulerian–Lagrangian framework consists of a RANS equation solver for the fluid flows with dynamic meshing, a morphological evolution model for the seabed, and a particle tracking model for sediment particles, detailed in Sections 2.1 to 2.3. The relationship among these components are summarized in Section 2.4.

2.1 Reynolds Averaged Navier–Stokes Equations for Fluid Flows

In this work, the fluid flows are described by using the incompressible RANS equations:

$$\frac{\partial U_i}{\partial x_i} = 0 \tag{1a}$$

$$\frac{\partial U_i}{\partial t} + \frac{\partial (U_i U_j)}{\partial x_i} = \frac{\partial}{\partial x_j}\left[\nu\left(\frac{\partial U_i}{\partial x_j} + \frac{\partial U_j}{\partial x_i}\right) - \overline{u_i' u_j'}\right] - \frac{1}{\rho}\frac{\partial P}{\partial x_i} + \overline{f_i} \tag{1b}$$

where U_i is the i^{th} component of Reynolds averaged velocity; x_i is the spatial coordinate; ρ is the fluid density; t is the time; P is the Reynolds averaged pressure; $\overline{f_i}$ indicate external body forces; ν is the kinematic viscosity of the fluid; $\overline{u_i' u_j'}$ is the Reynolds stresses, which is an unclosed second-order correlation term of velocity fluctuations.

In this study, the widely used two-equation *k*–*ω* model (Wilcox 1998) is employed to provide closure for the turbulent stresses in the RANS equations above. In this model, transport equations for the turbulent kinetic energy k and specific dissipation rate ω are solved. The turbulent viscosity, obtained from $\nu_t = k/\omega$, is used to compute the Reynolds stresses according to the Boussinesq eddy-viscosity assumption (Wilcox 1998):

$$-\overline{u_i' u_j'} = \nu_t\left(\frac{\partial U_i}{\partial x_j} + \frac{\partial U_j}{\partial x_i}\right) - \frac{2}{3}k\delta_{ij}, \tag{2}$$

where δ_{ij} is the Kronecker delta. Standard coefficients recommended in the literature are used for the *k*–*ω* model (Wilcox 1998).

2.1.1 Eulerian Modeling of Erosion, Deposition, and Morphological Evolution

The modeling of morphological evolution of seabed poses a significant challenge because of the complexity involved in the sediment transport processes. Depending on the flow regime, sediment transport can take various forms, e.g., bed load, suspended load, and wash load. In the bed load transport, various forms of sediment particles movement can occur, including sliding, rolling, and saltation. Due to the vastly different physical mechanisms in the different sediment transport regimes, it is difficult to represent the process in a unified model valid for all regimes. As such, most previous work of sand dune migration as mentioned in Section 1 focused on specified regimes of sediment transport. For example, Kraft et al. (2011) focused on the influence of suspended load, while Niemann et al. (2011) studied bed load transport. A dimensionless parameter used to characterize sediment transport regimes is Rouse number, defined as:

$$Ro = \frac{w_s}{\kappa u_\tau} \tag{3}$$

where w_s is the sediment particle settling velocity; $\kappa = 0.4$ is the von Kármán constant; $u_\tau \equiv \sqrt{\tau_0/\rho_w}$ is the friction velocity, where τ_0 indicates the magnitude of bed shear stress; ρ_w is the density of water. The flows of concern in this study have Rouse numbers smaller than 3. At this Rouse number suspension load is the dominant part of the total sediment transport (Wang et al. 1994), and thus we focus primarily on suspended load in the present work.

In the suspended load transport regime, the main mechanisms that are responsible for morphological evolutions identified in this work are erosion and deposition, the models of which are detailed in Sections 2.2.1 and 2.2.2. When erosion and deposition cause the bed slope to exceed its repose angle α_r, seabed instability occurs. This mechanism must be accommodated to represent realistic seabed morphological evolutions. In this work, we propose a new efficient diffusion model for sediment avalanching, which is discussed in Section 2.2.3. Finally, the morphological evolution equation accounting for erosion, deposition, and avalanching mechanisms are presented in Section 2.2.4.

2.2.1 Model for Seabed Erosion Fluxes

Van Rijn (1984a) performed experiments in steady flow over a flat bed to study the relationship between bed erosion and shear stresses, and identified the following formula for erosion rate q_e(eroded mass per unit area and time):

$$q_e = \begin{cases} 0.00033\left(\frac{\theta - \theta_c}{\theta_c}\right)^{1.5} \frac{(s-1)^{0.6} g^{0.6} d_p^{0.8}}{\nu^{0.2}} & \text{if } \theta \geq \theta_c \\ 0 & \text{if } \theta < \theta_c \end{cases} \tag{4}$$

where θ is the Shields parameter defined as:

$$\theta = \frac{u_\tau^2}{(s-1) g d_p}; \tag{5}$$

the Shields parameter can be considered as a dimensionless form of seabed shear stress; θ_c is the critical Shields parameter, taken as 0.09 according to the diagram of Madsen and Grant (1976), $s = \rho_p/\rho_w$ is the ratio between particle density ρ_p and water density ρ_w; g is the magnitude of the gravitational acceleration; d_p is the particle diameter.

It is assumed that the erosion function in Eq. (4) can be extended to unsteady flow by replacing θ with the time-dependent Shields parameter $\theta(t)$. Moreover, although this erosion function is determined from experiments using sand with the grain size from 0.13 mm to 1.5 mm, Kraft et al. (2011) used this function to study the sediment transport for the grain size at 0.1 mm. In their work, the simulated erosion agreed well with the experimental results. As such, this erosion function is adopted in the present study.

It is noted that the erosion flux in Eq. (4) provides only the information of the total eroded mass of the sediment particles at a given time. The initial conditions (i.e., the initial location and initial velocity) of the Lagrangian particles are not explicitly indicated by the erosion flux. The initial trajectory of particles when they are eroded from the seabed with different initial conditions is simulated by van Rijn (1984a) and validated against the experimental results of Fernandez Luque and van Beek (1976). Therefore, in this work the initial velocities of the eroded particle are determined based on van Rijn's studies.

2.2.2 Calculation of Sediment Deposition Fluxes

Empirical deposition models have been frequently used in previous studies where particle concentration equations are solved to model the suspended load transport (e.g., Giri et al. 2006; Niemann et al. 2011; Kraft et al. 2011). In the current work, Lagrangian models are used to represent each individual particle (or a group of particle, same hereafter; detailed in Section 2.3.4). Deposition occurs when a particle impacts on the seabed. This is illustrated in Figure 1(a). Therefore, deposition can be directly computed from the Lagrangian motion of the particles, and an empirical deposition model is not needed. Specifically, at each time step, the number of particles impacting on the seabed is recorded. The location of impact and thus the corresponding cells (indicated as filled squares in Figure 1(b)) in the mesh used for the discretization of the morphological evolution equation (7) can be identified. With this information, the source term q_d can be computed and used for the update of Eq. (7).

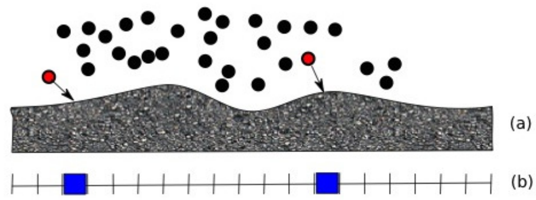

Figure 1 (a) Schematic showing sediment particles impacting on the seabed, leading to deposition.
(b) The mesh used for the discretization of the morphological evolution equation. This figure illustrates that the deposition flux q_d can be directly computed from the Lagrangian particle model, and an empirical deposition model is not needed.

It is assumed in this study that a sediment particle deposit on the seabed after the impact without rebound. This is a reasonable assumption for the particle diameters (0.1 mm) considered here. For larger particles (e.g., those with diameters larger than 2 mm), elastic rebound may be important and need to be considered (Nabi et al. 2013a). Although not explored in the current study, more sophisticated models such as elastic rebound or rebound with damping, can be implemented into the Lagrangian particle modeling framework in a straightforward manner.

2.2.3 Diffusion Model for Sediment Avalanching

As mentioned above, when erosion and deposition cause the bed slope to exceed the repose angle α_r of the seabed, instability occurs, i.e., sediment moves in the form of sliding or avalanching to reduce the local bed slope angle to α_r. The avalanching process should be modeled to allow for simulations of realistic seabed morphological evolutions. In previous work (Niemann et al. 2011), a sand slide routine has been used to represent the avalanche process. Specifically, when the slope angle of a surface becomes larger than α_r (see surface BC in Figure 2), the vertical coordinates of the nodes of this surface (B and C in Figure 2) are adjusted (to B' and C') to bring to slope angle down to αr while conserving the sediment volume. Effectively, this procedure is allowing the sand to slide down within the same computational cell. However, this adjustment can cause the slope angle of neighboring cells (AB and CD) to increase and possibly to exceed α_r. Therefore, the sand slide routine needs to be repeated for the neighboring cells of the adjusted cells. This process continues until all the slope angles for all cells are below α_r. The complexity of this routine is $O(M^2)$, where M is the number of cells whose slope angles are adjusted in the first round (Jacobsen 2011). When M is large, this routine may become inefficient. Moreover, this discrete filtering procedure does not fit well in the continuum modeling framework based on partial differential equations.

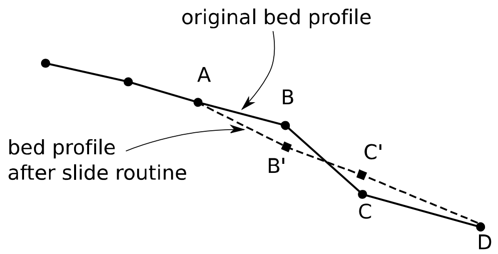

Figure 2Sand sliding procedure used in the literature to avoid local slope angle exceeding the repose angle.

In the current work, we propose an efficient sediment avalanching scheme by adding a diffusive flux q_s to the morphological evolution equation. This flux is formulated as follows:

$$q_s = \begin{cases} \frac{\partial}{\partial x}\left(\gamma_s \frac{\partial h}{\partial x}\right) & if\ \frac{\partial h}{\partial x} \geq \tan(\alpha_r) \\ 0 & if\ \frac{\partial h}{\partial x} < \tan(\alpha_r) \end{cases} \quad (6)$$

where γ_s is a diffusion coefficient, an algorithmic parameter to be determined. Note that the flux q_s (due to sediment avalanche) is only nonzero when the local angle of the bed surface exceeds the repose angle α_r. The coefficient γ_s should be chosen large enough for the sliding to occur sufficiently fast, but not so large as to cause computational instability.

A test case similar to the one studied by Nabi et al. (2013a) is used to validate the proposed avalanche model and to calibrate the parameter γ_s. A two-dimensional sand dune with initial section shown in Figure 3 is studied. The size of the domain is chosen to be 2 m, and the initial height of the dune is 0.5 m. The maximum angle in the initial slope of the dune is 75°; α_r is taken as 30° following Chanson (2004). Quiescent flow is assumed, and thus no sediment erosion or deposition occurs. Figure 3 shows snapshots at two time instances during the sediment avalanche, demonstrating good agreement with the simulation by Nabi et al. (2013a) when γ_s = 1.0×10^{-4} m^2/s is used. Also, when the angle of the dune reaches α_r, the avalanche stops as expected, and the slope angle remains α_r afterwards. Compared with the sand sliding routine (Niemann et al. 2011), the present model not only provides an accurate solution to the avalanche of the dune but has reduced computational cost. Moreover, it is an advantage that the diffusion flux can be discretised in the same framework as other terms in the morphological evolution equation.

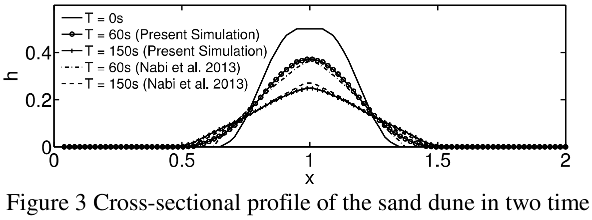

Figure 3 Cross-sectional profile of the sand dune in two time instances during avalanching processes. Only sliding is considered; the result is compared to Nabi et al. (2013a). The sliding stops when the angle of dune reaches the repose angle α_r.

2.2.4 Model for Morphological Evolution

Summarizing the erosion, deposition, and avalanching models presented above, the morphological evolution of the seabed can be described as following:

$$\theta = \frac{\partial h}{\partial t} = \frac{1}{\cos\alpha}\frac{q_d - q_e}{1-\varphi} + q_s, \quad (7)$$

where h is the bed elevation with respect to a specified datum; α is the local angle of bed slope; q_d is the rate of deposition; q_e is the rate of erosion; φ is the seabed porosity; q_s is the rate of sliding. Here, we convert the morphological change from the normal direction n to the vertical direction n by multiplying $1/\cos(\alpha)$, where α is the local slope angle, i.e., the angle between n and n' as shown in Figure 4. The flux q_s is included in the morphological evolution equation to account for the sliding of the dune when slope angle exceeds the repose angle, as described in Section 2.2.3.

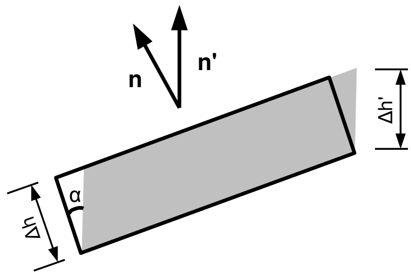

Figure 4 Projection that changes the direction of morphological change. The grey and empty parallelograms have the same area but differ in direction. To update the deformation in the vertical direction, $\Delta h' = \Delta h/\cos(\alpha)$ is used instead of Δh. This projection does not change the total area of erosion or deposition.

To update the bed elevation in the Eulerian–Lagrangian framework, the morphological evolution equation needs to be solved. Similar to previous works (e.g., Jacobsen et al. 2014), a separate 2D mesh, using finite volume method, is constructed at the seabed. The mesh used to solve Eq. (7) is implemented for curved surfaces in space (Tukovic et al. 2012), which is referred to as finite area method. This method has been proved to be well-suited for solving the morphological change at the seabed (Jacobsen et al. 2014).

2.2.5 Dynamic Mesh for the RANS Solver

In current-induced morphological evolution of sand dunes, the interactions between the hydrodynamics and morphological evolution can be significant. Specifically, the logical evolution of the seabed induced by the flow changes the boundaries of the fluid flow, which in turn changes the forces exerted on the seabed. To capture the interactions between the hydro- and morpho-dynamics of the coupled system, one needs to update the computational mesh used for the hydrodynamic simulation as the morphological pattern evolves.

The overall idea of dynamic mesh is illustrated in Figure 5. It can be seen that the mesh deforms globally to fit the evolving bathymetry as the erosion and deposition gradually modify the seabed configuration. The exact displacement v of each grid point can be determined by solving an elliptic partial differential equation (i.e., a diffusion equation) (Jasak et al. 2006; Jasak et al. 2009):

$$\nabla \cdot (\gamma_m \nabla \mathbf{v}) = 0 \quad (8)$$

where $\nabla \cdot$ and ∇ denote divergence and gradient operators, respectively; γ_m is the diffusion coefficient controlling the smoothing of mesh displacements within the computational domain.

There are multiple ways of choosing this coefficient. In this work the following scheme is adopted:

$$\gamma_m = \frac{1}{\gamma^2} \tag{9}$$

where γ is the distance from the center of the cell to the surface of the seabed boundary.

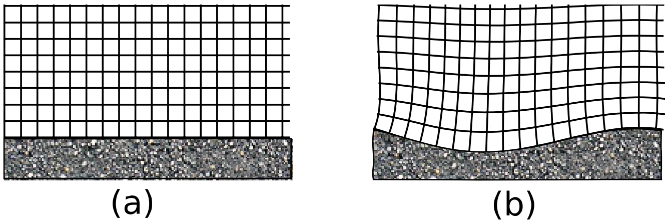

Figure 5 A schematic of the dynamic meshing procedure, which can accommodate the influence of morphological changes on the hydrodynamics in coupled hydrodynamic–morphological simulations. (a) Initial mesh and seabed geometry (shaded); (b) deformed mesh to fit the bathymetry after seabed erosion and deposition.

The smoothing property of the elliptic equation leads to the effect that the mesh movement is largest at the seabed boundary, and gradually diminishes further away from the boundary. When a new mesh is obtained via deformation based on current bathymetry, the state variables associated with the old mesh are mapped to the new one. To account for the mesh displacement, the original conservation equations for mass, momentum, and turbulent quantities need to be modified to accommodate the Geometrical Conservation Law (e.g., Thomas et al. 1979; Farhat et al. 2001). This is achieved by subtracting the local mesh velocity v from the transport velocities in the flux terms (see, e.g., Eq (2) in Luo et al. 2004). Finally, it is noted that in the dynamic meshing procedure no cells are added or removed in the dynamic meshing scheme, and the topology of the mesh does not change.

2.1 Lagrangian Modeling of Suspended Sediment Particles

2.1.1 Equations of Particle Motion

The motion of particles is influenced by the fluid flow, but the flow is not influenced by the particles, which is referred to as one-way coupling. This is justified by the fact that the particle volume fraction is very low, and their influences on the fluid flow are small. The movement of each particle is described by the Newton's second law. The various forces acting on the particles, including drag, lift, and buoyancy are obtained from physical reasoning or empirical correlations in the literature. Specifically, neglecting particle rotation and inter-particle collisions, the following equations are solved for each individual particle:

$$m_p \frac{\partial \mathbf{U}_p}{\partial t} = \mathbf{F}_G + \mathbf{F}_D + \mathbf{F}_L \tag{10a}$$

$$\frac{\partial \mathbf{x}_p}{\partial t} = \mathbf{U}_p \tag{10b}$$

where m_p is the mass of the particle; $\mathbf{U}_p$ and $\mathbf{x}_p$ are the particle location and velocity, respectively; $\mathbf{F}_G$, $\mathbf{F}_D$ and $\mathbf{F}_L$ are submerged weight of the particle, drag force and lift force acting on the particle respectively. By integrating Eq. (10) in time for each particle, the velocity and trajectory for all particles in the system can be obtained. The mass of a spherical particle accounting for the added mass can be expressed as:

$$m_p = \frac{\pi}{6}\left(\rho_p + C_m \rho_w\right) d_p^3 \tag{11}$$

where ρ_p is the density of sediment particle; C_m = 0.5 is the added mass coefficient; ρ_w is the density of water.

The submerged weight $\mathbf{F}_G$ is obtained as following:

$$F_G = \frac{\pi}{6}\left(\rho_p - \rho_w\right) d_p^3 g \tag{12}$$

where $\mathbf{g}$ is the gravitational acceleration. The following empirical formulation for spherical particles is adopted for the calculation of drag force $\mathbf{F}_D$ (Stiesch 2003):

$$\mathbf{F}_d = \frac{1}{2} C_d \rho_w A_p \left|\mathbf{U}_{w@p} - \mathbf{U}_p\right| \left(\mathbf{U}_{w@p} - \mathbf{U}_p\right) \tag{13}$$

where $A_p = \pi d_p^2/4$ is the frontal area of the particle; $\mathbf{U}_{w@p}$ is the water velocity interpolated to the position of the particle, or equivalently the water velocity "seen" by the particle. The determination of this quantity requires reconstruction of instantaneous flow field velocities, which will be further detailed in Section 2.3.3. The following correlation is used for the drag coefficient C_d (Stiesch 2003):

$$C_d = \begin{cases} \frac{24}{Re_p}\left(1 + \frac{1}{6} Re_p^{\frac{2}{3}}\right) & \text{if } Re_p \le 1000 \\ 0.424 & \text{if } Re_p > 1000 \end{cases} \tag{14}$$

where $Re_p = d_p \left|\mathbf{U}_{w@p} - \mathbf{U}_p\right| / \nu$ is the particle Reynolds number.

The velocity gradient in the flow field can lead to the lift forces on a spherical particle. This is because the velocity gradient will result in a flow deflection at the particle surface so that the flow velocity, and consequently the pressure, on one side can be different from the other side. The pressure difference leads to the lift forces. This effect is modeled as (van Rijn 1984b; Saffman 1965):

$$F_l = C_l \rho_w \nu^{0.5} D^2 \left(\mathbf{U}_p - \mathbf{U}_{w@p}\right) \times \nabla \mathbf{U}_{w@p} \tag{15}$$

where × indicates the cross product of two vectors, and C_l = 1.6 is the lift coefficient.

2.3.2 Initialization of Suspended Particles in Flow Field

Although all suspended sediment particles in the flow field are represented in a Lagrangian framework, the sediment of the seabed are not explicitly represented. Instead, bed elevation is used to represent the bathymetry at each location of the seabed, as can be seen from Eq. (7). Consequently, the "life" of a particle starts only when it is suspended, or eroded from the seabed. In this case, the particle will be created. The life of the particle ends when the particle impact on the seabed (see Section 2.2.2), i.e. when it deposits. While the deposition involves deleting the particle from the system, which is straightforward, the creation of particles is not trivial. The difficulty lies in the initialization of locations and velocities of the suspended particles. Physically, at the moment when a particle leaves the seabed, its distance to the seabed and its initial velocity are infinitesimal by definition. Subsequently, the hydrodynamic forces acting on the particle would lift it away from the seabed and help it enter the flow field. However, the flow physics within the boundary layer of the seabed are not well resolved in this framework, and thus the hydrodynamic forces on these particles when they are first eroded are not accurate. As a result, many of these particles would have initial downward movements, causing them to deposit immediately after being created. This behavior is physically incorrect and computationally inefficient.

To address this issue, it is desirable that the newly created particles have initial locations at certain finite distance d_0 above the seabed, and that they have a certain finite initial velocity u_0. The parameters d_0 and u_0 would serve as initial conditions for Eq. (10). These are essentially computational parameters, although their determinations do have some physical justification. Under simplified flow conditions van Rijn (1984b) derived the trajectory of an eroded particle, including the time series of its location $\mathbf{x}_p(t)$ and velocity $\mathbf{U}_G(t)$, which are illustrated in Figure 6. Based on his study, in this work we choose the parameters as d_0 = 0.6 d_p, and the vertical and streamwise components of $\mathbf{U}_0$ are both $2u_\tau$, creating the particle at a small distance away from the point where the particle physically leaves the seabed. However, choosing the exact location on the trajectory to start is somewhat arbitrary. Since the velocity gradient is large in the near wall region, small variations of the particle initial conditions d_0 and $\mathbf{U}_0$ may result in large differences in the saltation distance and initial trajectories of the particles. Hence, further studies of these initial conditions are needed.

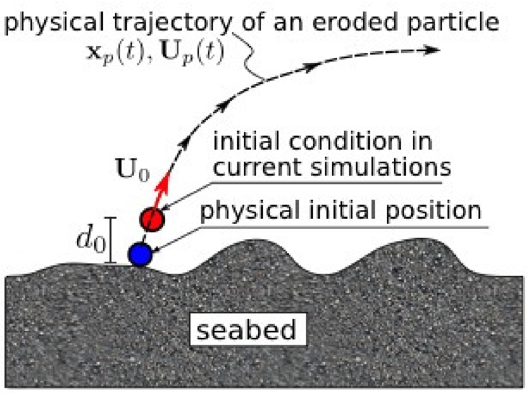

Figure 6 A schematic showing the trajectory, i.e. time history of locations and velocities ($\mathbf{x}_p(t)$ and $\mathbf{U}_G(t)$), of an eroded particle. Also illustrated are the physically correct initial condition of a particle (blue) and the strategy used in this simulation (red) by starting at certain distance d_0 above the seabed with a finite initial velocity $\mathbf{U}_0$.

2.3.3 Sediment Dispersion

When tracking particle motions in turbulent flows, the instantaneous velocity field $\mathbf{u}$ of the flow is needed, which is, however, not available from the RANS equations. The fluid velocity $\mathbf{U}_{u@p}$ seen by the particles needs to be interpolated from $\mathbf{u}$. As RANS equations only describe the mean flow velocity $\mathbf{U}$, some reconstructions and modeling are needed to obtain the instantaneous velocity field.

In this work, it is assumed that the velocity fluctuation $\mathbf{u}_t$ conforms to a Gaussian distribution (O'Rourke 1989; Amsden et al. 1989; Bharawaj et al. 2009), i.e., the probability density function of $\mathbf{u}_t$ is

$$P(\mathbf{u}_t) = \frac{1}{\tilde{u}\sqrt{2\pi}} \exp\left(-\frac{\mathbf{u}_t^2}{2\tilde{u}^2}\right) \tag{16}$$

where $\tilde{u} = \sqrt{2k/3}$ is the fluctuation velocities inferred from k according to isotropic turbulence assumption. The instantaneous velocity of the fluid is thus computed as $\mathbf{u} = \mathbf{U} + \mathbf{u}_t$. This reconstructed velocity u will be interpolated to obtain $\mathbf{U}_{u@p}$, which is then used for the calculation of particle drag forces as shown in Eq. (13).

Since RANS equations do not explicit resolve the instantaneous velocity of the flow field, we have to reconstruct this information from statistical quantities in the *k*–*ω* model. Due to the lack of information, it is assumed that the reconstructed fluid velocity $\mathbf{u}_t$ is piecewise constant within the reconstructed "eddy" (O'Rourke 1989) until it is updated. As such, the fluid velocity seen by a particle is only updated when the life of the eddy within which the particle resides ends, or when the particle moves to another eddy, whichever occurs first. The time interval t_c for which the particle-seen velocity is updated can be defined as (Bharadwaj et al. 2009):

$$t_c = \min\left(\frac{k}{\varepsilon}, \frac{C_{ps}k^{\frac{3}{2}}}{\varepsilon|\mathbf{U}_{rel}|}\right) \tag{15}$$

where C_{ps} = 0.164 is a constant; $\mathbf{U}_{rel} = \mathbf{U}_p - (\mathbf{U} + \mathbf{u}_t)$ is the relative velocity of the particle with respect to instantaneous velocity of the turbulent flow as seen by the particle; $\mathbf{U}$ is the Reynolds-averaged velocity obtained from Eq. (1); $\varepsilon = \beta^* k\omega$ is turbulent dissipation with constant β^* = 0.09. Detailed explanations of the instantaneous fluid velocity seen by a particle can be found in the reference (e.g., O'Rourke 1989).

2.3.4 Computational Representation of Sand Particles

In field-scale modeling of sand dune migration and sediment transport, the number of sand particles in the flow can be very large. Indeed, a handful of sand can contain millions of fine particles. To represent each of these particles individually in the numerical model would be prohibitively expensive computationally, and this is indeed unnecessary in most cases. After all, we are more interested in the collective behavior of the sediments in the flow than in the individual trajectory of each particle. These behaviors include inceptive motion, transport, dispersion, and deposition, among others. To reduce the computational cost of particle tracking and updating, a concept called a "parcel", or equivalently a "computational particle", is used in the current framework, which was originally introduced in the simulation of fuel sprays in internal combustion engines (Amsden et al. 1989). Each parcel in the current model (indicated as large dots in Figure 7) represents a group of physical particles (indicated as small dots in Figure 7) with similar or identical characteristics such as diameters, densities, velocities, and locations. If the group of particles to be represented by a parcel are identical, the intensive quantities (e.g., diameter, density) of the parcel are taken to be the same as those of the particles, while the extensive quantities (e.g., mass) of the parcel are the sum of those of the particles. When the particles to be represented are not identical but have a certain distribution, the intensive quantities of the parcel can be considered as the mass weighted mean of the particle quantities of the particle group.

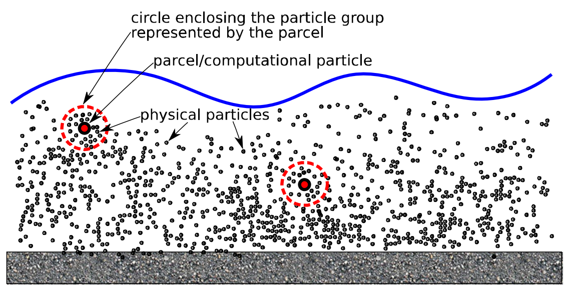

Figure 7 Computational representations of sand particles. Parcels (indicated as large dots; only two are shown for clarity), also called computational particles, are used to represent a group of physical particles (indicated as small dots in dashed circles) with similar or identical characteristics. This flexible representation enables the numerical modeling to maintain a reasonable computational cost that is independent of the number of physical particles in the system.

This representation of physical particles can be interpreted in a Monte Carlo framework, since each computational particle can also be considered as a "realization" of one of the many physical particles. In the Monte Carlo interpretation, it also is possible to use multiple computational particles to represent one physical particle, with each computational particle being a possible state of the physical one. This flexible representation of physical particles enables the Lagrangian particle modeling to be conducted with reasonable computational cost, independent of the number of physical particles in the fluid–sediment system. Moreover, the number of physical particles represented by each parcel can be determined individually, and it may also vary with time.

2.4 Summary of the Eulerian–Lagrangian Framework

As a summary of the proposed modeling methodology, the relationship and interactions among the modules presented in Sections 2.1 to 2.3 are illustrated in Figure 8. The specific algorithm of the coupling between hydrodynamics and sediment transport is shown in Algorithm 1. It is emphasized that the fluid-particle interaction is one-way; that is, while the fluid exert drag and lift forces on the particles and causes erosion and deposition of particles from the seabed, the modification of fluid mass conservations due to presence of the particles and the particle forces on the fluid are ignored. This is justified by the assumption that the volume fractions of particles are small. However, as is evident from the loop in Figure 8, the fluid motions are indirectly influenced by the particles. Specifically, the particle movements lead to morphological evolution of the seabed, which changes the boundaries, computational domains, and the mesh of the fluid flow solver.

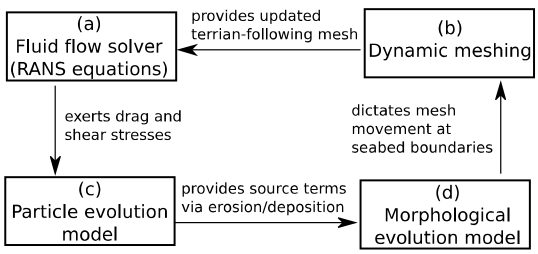

Figure 8 Relationship and interactions among the four major modules in the current numerical framework, starting from upper left: (a) fluid flow solver (Eq. (1a)); (b) particle evolution model (Eq. (10)); (c) morphological seabed evolution model (Eq. (7)); and (d) dynamic meshing model (Eq. (8)). The relationship and interactions among these modules are indicated with arrows and texts.

1. Initialize fields for the fluid flow;
2. Initialize particles states if any;
for *each time step* **do**
- **1.** Solve Reynolds-averaged momentum and pressure equations for U and P;
- **2.** Solve equations for turbulent quantities;
- **3.** Compute particle forces and bed shear stresses;
- **4.** Evolve particles according to Eq. (10); compute erosion and deposition fluxes q_e and q_d;
- **5.** Update bed elevation according to Eq. (7);
- **6.** Perform sediment avalanche procedure as needed;
- **7.** Deform fluid flow solver mesh according to updated seabed bathymetry;

end

Algorithm 1 Overall algorithm of the Eulerian–Lagrangian modeling framework as implemented in this work.

In the works of Chang and Scotti (2003) and Escauriaza et al. (2011), the morphological changes of the seabed were ignored, and the particle dispersion due to subgrid scale of turbulent flow was not considered. The current study models the morphological change via dynamic meshing and accounts for the particle dispersion by reconstructing instantaneous velocities. In the Lagrangian framework proposed by Nabi et al. (e.g., Nabi et al. 2013a; Nabi et al. 2013b), a discrete-element model was used to treat the pickup and deposition, and the motion of every particle was modeled. Consequently, the total computational costs of their numerical simulations are relatively high, particularly for systems with a large number of particles. In contrast, we use a Monte Carlo framework to represent a number of particles of similar characteristics with "parcels", significantly reducing the computational costs and increasing the flexibility of the modeling framework.

3. IMPLEMENTATION AND NUMERICAL METHODS

The proposed Eulerian–Lagrangian framework is implemented based on OpenFOAM (e.g., OpenCFD 2013), an open-source, object-oriented platform for computational fluid dynamics. The developed solver takes advantage of existing RANS solvers, discretization of differential operators, as well as dynamic mesh solver and particle tracking capabilities implemented in OpenFOAM. Parallel computing, which is a built-in capability of OpenFOAM, is employed to improve the performance of the simulations. The dynamic meshing procedure implemented OpenFOAM is used in the current modeling framework.

The RANS equations and morphological evolution equation are discretised using finite volume method on a collocated grid. Second-order upwind schemes are used for convective terms. Second-order central schemes are used for other terms. A second-order implicit scheme is used for time integration. PISO (Pressure Implicit with Splitting of Operator) algorithm (Issa 1986) is used to prevent velocity–pressure decoupling on collocated grids.

4. NUMERICAL SIMULATIONS

The developed Eulerian–Lagrangian model is used to simulate two representative cases: (1) the turbulent flow over a wavy bottom with fixed bed at a relatively low Reynolds number, and (2) the formation and development of a movable sand dune in the flow at a higher Reynolds number. The purpose of the first case, presented in Section 4.1, is to validate and assess the performance the fluid flow solver on the dune-shaped geometry without introducing the complexity from sediment transport, morphological evolution, and dynamic mesh. Benchmark solutions from DNS and previous RANS simulations are used to assess the RANS simulations in this work. The second case, presented in Section 4.2, serves as a comprehensive test of the Eulerian–Lagrangian solver coupling all the modules discussed in Section 2. In this case, the time-evolution of the sand dune under the action of currents is studied; statistical information of particles, including their residence time and velocity distribution is presented.

4.1 RANS Simulations of the Fluid Flow

In this case, the flow over a periodic sinusoidal dune is studied and compared with benchmark results (Knotek et al. 2014; Maaß et al. 1996; Yoon et al. 2009). The profile of the sinusoidal dune, shown in Figure 9, can be described as:

$$h_0(x) = A \sin\left(\frac{2\pi x}{L}\right) \tag{18}$$

where h_0 is the bed elevation; A and L are the amplitude and wave length, respectively, of the dune with $A = 0.05L$; x is the horizontal, streamwise coordinate. The average height of the computational domain is $H = L$. See Figure 9 for details of the domain. The

Reynolds number $Re = U_b L / \nu$ defined based on the wave length L and volume-averaged velocity U_b is 6760.

The simulation of this case is performed on a two-dimensional, body-conforming, topologically structured finite volume mesh with a resolution of 60 (streamwise direction) × 80 (wall-normal direction) cells. The mesh is stretched towards both the top and the bottom walls, leading to higher resolution near the wall boundaries and coarser mesh in the channel center. To evaluate the adequacy of the mesh resolution, the dimensionless wall distance $y^+ \equiv u_\tau y / \nu$, defined for the cells immediately next to wall boundaries with y being the distance from cells centres to the nearest wall, is computed and presented in Figure 10. It is noted that when calculating y^+, the friction velocity from DNS data (Yoon et al. 1996) are used instead of those from the present RANS simulation. It can be seen that the maximum y^+ value is approximately 2.3. Hence, the boundary layer is properly resolved with the first layers of near-wall cell well within the viscous sub-layer, and thus no wall function is needed.

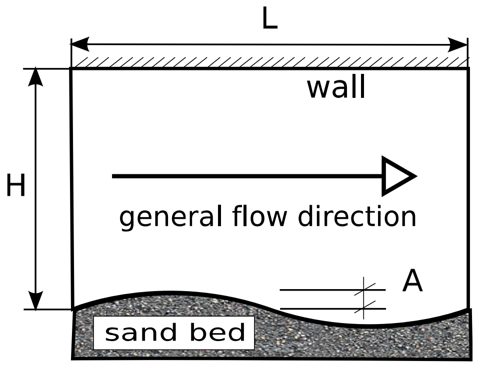

Figure 9 Schematics diagram of the sinusoidal dune (showing the wave length L and amplitude A) and the computational domain (showing the average domain height) for the fixed dune simulations. The initial computational domain for the sand dune migration simulations is the same as illustrated here, except that the height H has a different value than that in the fixed dune case, and that the computational domains changes as the sand dune evolves.

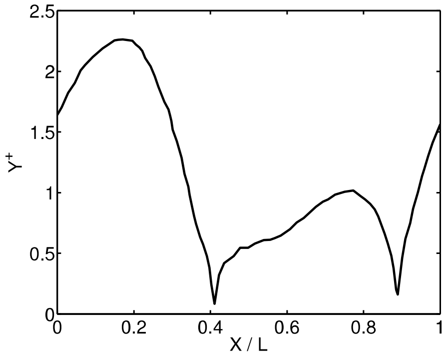

Figure 10 Evaluation of mesh resolution for the flow over a sinusoidal dune at a Reynolds number *Re* = 6760, showing the *y*+ value for cells immediately next to the sand bed. The maximum *y*+ value is smaller than 2.3, demonstrating the adequacy of the mesh resolution.

The shear stresses on the lower boundary, normalized by ρU_b^2, is displayed in Figure 11(a), the maximum positive shear stress on the bottom is 1.16×10^{-2}, located at $x/L = 0.2$; the maximum negative shear stress is -3.5×10^{-3}, located at $x/L = 0.85$. The shear stress grows gradually on the windward side of the dune, and decreases on the leeward side. The separation and reattachment points can be found by identifying the points at which the boundary shear stress crosses the zero axis from the positive to the negative side, and from the negative to the positive side, respectively. See the annotations in Figure 11(a). The region in between the separation and reattachment points is the recirculation region, that is, in this region the flow goes in the opposite direction as in the free stream. This is also indicated in Figure 11(a). Usually in these regions the flow tends to recirculate and has lower energy levels. Consequently, suspended sediment particles in the flow are trapped here and are more likely to settle and accumulate. From Figure 11(a), locations of separation and reattachment points are identified and presented in Table 1. It can be seen that although the locations of the separation and reattachment points do not agree well with the experimental data (Hudson et al. 1996), the agreement with the DNS results (Yoon et al. 1996) and with the RANS simulation results by Knotek et al. (2014) is satisfactory. Note that the RANS simulations by Knotek et al. (2014) also used *k–ω* turbulence model, and thus the good agreement of current results with theirs is expected.

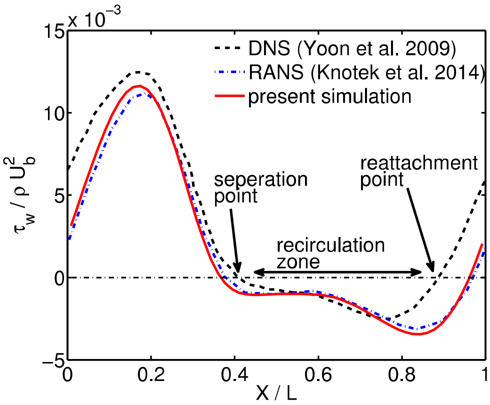

(a) Wall shear stress

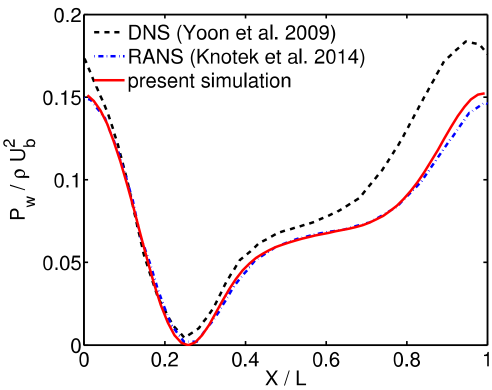

(b) Pressure

Figure 11 (a) Wall shear stress and (b) pressure on the lower boundary, normalized by ρU_b^2. The results are compared with Knotek et al. (2014) and Yoon et al. (2009) (partly overlapped with the present results).

Table 1 Predicted separation and reattachment points by using a RANS solver with *k–ω* model, compared with experimental data (Hudson et al. 1996), DNS (Yoon et al. 2009), and other RANS simulations (Knotek et al. 2014) in the literature.

	separation (x/L)	**reattachment** (x/L)
Experiments (Hudson et al. 1996)	0.47	0.83
DNS (Yoon et al. 2009)	0.39	0.87
RANS (Knotek et al. 2014)	0.38	0.96
Present simulation	0.38	0.96

The pressure distribution on the wavy boundary, normalized by ρU_b^2, is shown in Figure 11(b). The maximum and minimum pressure values are located at x/L == 1.0 and 0.25, respectively. The differences between the maximum and minimum normalized pressure is 0.15. Similar to the shear stress results, Figure 11(b) shows that the pressure profiles on the lower boundary obtained from the two RANS simulations (i.e., from this study and that of Knotek 2014) almost coincide with each other, and that the RANS simulation results also agree reasonably well with the DNS results except for some discrepancies near the reattachment point.

The profiles of streamwise velocities, normalized by the volume-averaged velocity U_b, at different sections, x/L = 0.35, 0.55, 0.75, and 0.95, in the recirculation zone of the channel is shown in Figure 12(a). Compared with the benchmark solution, the velocity profiles in the streamwise direction agree well, and the inflection points are well predicted, although the vertical velocity profiles at x/L = 0.75 and 0.95 are not well predicted by either RANS simulations. In spite of some discrepancies in the predicted vertical velocities, due to the much smaller magnitude of the vertical velocity component compared with the streamwise component, the overall flow pattern is still well captured by the RANS simulations.

Based on the comparisons conducted in this case, it is concluded that the present simulations agree very well with the RANS simulations of Knotek et al. (2014). Overall, the agreement with benchmark data including DNS results and experimental data are also satisfactory, although some discrepancies do exist, especially near the reattachment region. The discrepancies between RANS results and those of DNS and experimental data and are attributed to the intrinsic, well-known limitations of the RANS modeling methodology, which are not further discussed. Here, it suffices to conclude that the RANS solver used in this study and the setup of the cases are verified and validated.

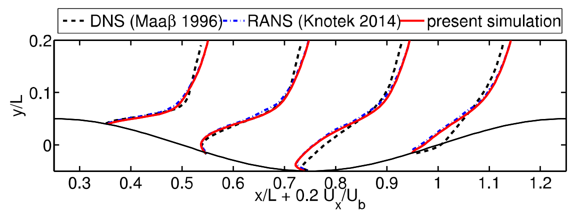

(a) Streamwise velocity

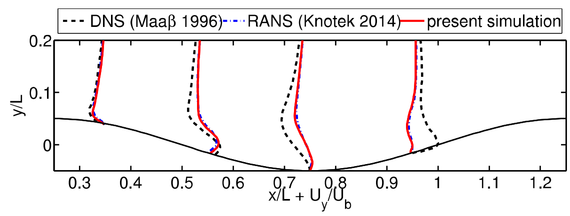

(b) Vertical velocity

Figure 12 Velocity profiles in the (a) streamwise and (b) vertical directions near the wavy bottom boundary, normalized by the volume-averaged velocity U_b. The results of the present simulation are compared with Knotek et al. (2014) and Maaß et al. (1996). The wavy line denotes the bottom profile.

4.2 Current Induced Sand Dune Migration

After the verification and validation performed above, the Eulerian–Lagrangian framework developed in this work is used to simulate a dune deformation experiments performed by Haslinger (1993). The initial profile of the sand dune and the shape of the computational domain are the same as in the previous case, except for two notable differences. First, the channel height $H = 0.4L$ in the experimental setup is smaller than the previous case used to validate the RANS solver, where the channel height is $H = L$. Second, and more importantly, this case has a larger Reynolds number (Re = 33700) compared with the previous case. Consequently, DNS solutions are not available due to the high computational costs required by DNS for simulating high Reynolds number flows. Kraft et al. (2011) conducted Large Eddy Simulation (LES) for the flow field; the particle phase was described by solving a convection–diffusion equation for particle concentrations. The computational cost and accuracy of LES are generally lower than DNS but much higher than RANS.

Table 2 Parameters used in the sand dune formulation migration simulations in this study

Density of water (ρ_w)	$1000\ kg/m^3$
Particle density (ρ_p)	$2650\ kg/m^3$
Particle diameter (d_p)	$0.1\ mm$
Kinematic viscosity of water (ν)	$8.9 \times 10^{-7}\ m^2/s$
Porosity of seabed (φ)	0.30
Gravity (g)	$9.81\ m/s^2$
Volume-averaged velocity (U_b)	$0.50\ m/s$
Reynolds number (Re)	33,700
Cells in computational mesh	150 (horizontal) $\times$ 60 (vertical)
Number of computational particles	approximately 10,000

Due to the higher Reynolds number and smaller channel height in the case, the mesh resolution is adjusted accordingly to 150 (streamwise direction) × 60 (wall-normal direction). The y^+ values in this case are slightly higher than those in the $Re = 6760$ case. This is due to the fact that overly small cell-sizes cause difficulties in dynamic mesh procedures. However, the currently used mesh still has adequate near-wall resolution, and no wall functions are needed. We also note that the height $H = 0.4L$ of the computational domain in this case is smaller than that in the previous case ($H = L$).

4.2.1 Flow on Fixed Sand Dune

Before considering the movable bed with sediment transport and dynamic mesh, we first simulate the flow field in this case with a fixed bed. Since the bed shear stress play a critical role in bed erosion and sediment transport, the bed shear stress is presented. Considering that this case differs from previous case in Section 4.1 in two aspects, i.e., Reynolds number and channel height, it is difficult to distinguish the different contribution factors in the observed differences in the obtained results. Therefore, another case with $Re = 6760$ and $H = 0.4L$ are simulated, leading to the comparison among three cases: (1) $Re = 6760$ and $H = L$; (2) $Re =$ 6760 and $H = 0.4L$; and $Re = 33700$ and $H = 0.4L$. The comparison between Cases 1 and 2 highlights the contribution of varying channel height; the difference between Cases 2 and 3 demonstrates the influences of Reynolds number.

From Figure 13, the shear stresses on the bottom boundary are very similar between Cases 1 and 2, which have the same Reynolds number, although a slight decrease of the shear stress is observed downstream of the separation point. Meanwhile, the position of the separation point remains at $x/L = 0.38$ but the reattachment point is moving forward to $x/L = 0.92$. It can be concluded that the difference in channel height does not lead to significant changes in the distribution of bed shear stresses. On the other hand, comparison between Cases 2 and 3 suggest that with the same channel geometry but with the Reynolds number changing from 6760 to 33700, the maximum shear stress is reduced to 7.2×10^{-3}, with the location of peak shear stress shift downstream slightly. The shear stress in the recirculation zone is also reduced to -1.0×10^{-3}. The locations of flow separation are only slightly different between the cases 2 and 3, but the reattachment point moves towards upstream, from $x/L = 0.92$ to $x/L = 0.83$, leading to a significantly shorter recirculation zone.

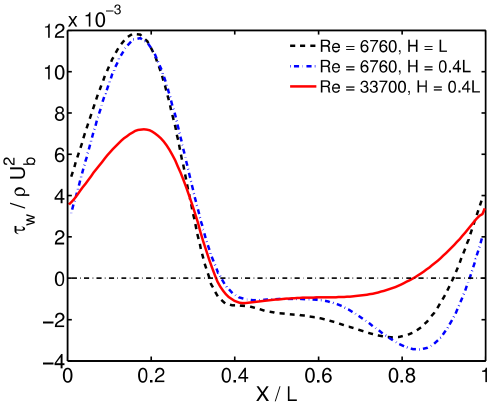

Figure 13 Comparison of wall shear stress distribution of different channel heights and Reynolds numbers. The results are normalized by ρU^2.

4.2.2 Development of Sand Dune

The initial geometry of the seabed is defined as Eq. (18). The time history of dune generation is displayed in Figure 14, the solid lines show the bed profile at different times, the dashed line show the trace of the movement of the crest. Although the crest should be taken as the highest point of the bed profile, there is no such a point but a flat region of high bed level at $tU_b/L = 80$. Therefore, the crest is not simply taken at the highest point but midpoint of the highest part. Since the crest of the dune reappears after $tU_b/L = 80$, the line connecting crest of the dune at every time from tUb/L = 40 to $tU_b/L = 80$ is not displaying the real movement of the dune. Hence, we simply connect the two crests at $tU_b/L = 40$ and 80 to display the movement of the crest during this period. From Figure 14, it can be seen that the dune starts deforming rapidly before $tU_b/L = 50$; after that, the deformation of the bed slows down, and the dune migrates with the flow at a constant velocity. The average velocity of the migration after $tU_b/L = 70$ is about 1.0×10^{-4} m/s, which agrees favorably with the results of Kraft et al. (2011).

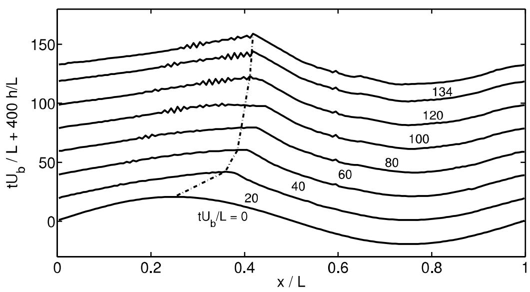

Figure 14 Formation of sand dune from an initial sinusoidal profile under current actions. The solid lines show the evolution of the dune structure over time; the dash line shows the migration of the crest of the dune.

After $tU_b/L = 134$, although the sand dune continues to evolve, the rate of migration is so small that the final equilibrium bed profile can be considered to be formed. It can be seen from Figure 15 that the final ripple profiles simulated by the current model agrees favorably with the results of other numerical simulations and physical experiments (e.g., Haslinger 1996; Kraft et al. 2011), especially at the region near the crest. The steepest angle of the dune simulated by the present model also agrees well with the experiment, indicating the capability of the proposed avalanche model. The agreement between the present simulation and the benchmark results is not very well with near the reattachment point. Moreover, the total volume of dune erosion and the distance of dune migration in the present work are slightly smaller than that observed in experiments (Haslinger 1996). These discrepancies are mainly caused by the inaccuracies of the RANS model in simulating the flow near the reattachment point.

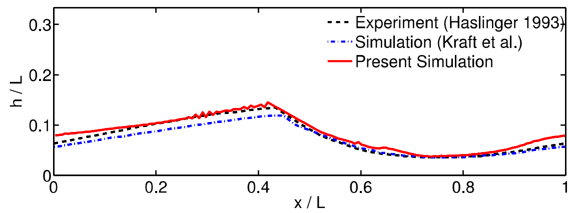

Figure 15 Comparison of the final bed profile of the present simulation with the results of experiment of Haslinger (1993) and the numerical simulation by Kraft et al. (2011).

Another difference between our simulations and those by Kraft et al. (2011) is the roughness upstream of the dune crest. Figure 15 shows this roughness in the final ripple profile. Convection of these roughness features in the flow direction can be observed in Figure 14 along with the migration of the sand dune. Since the wave lengths of these roughness features span only two cells, it is likely that these observed ripples are not physical features but numerical artifacts. These numerical oscillations can be easily damped by adding a small diffusion term. An explanation for this numerical oscillation is that the sink term of the morphological evolution equation (7) is due to the deposition. The deposition is caused by discrete particles impinging on the seabed, which have stochastic behaviors due to the dispersion described in Section 2.3.3. Therefore, the amount of deposition is not necessarily smooth spatially. The spatially non-smooth deposition amount leads to small-wave-number roughness as observed in Figs. 14 and 15. In contrast to standard morphological evolution equations purely or partly based on continuous field variables (Paola et al. 2005), in the current formulation there are no convection or diffusion terms that can smooth out the small-wave-number roughness. Note that the avalanche term is active only when the local bed slope exceeds the repose angle α_r, and thus it can only reduce roughness to α_r, but is not able to eliminate them completely. As explained in Section 2.2, only suspended load is considered in the simulations presented in this work. To confirm the analysis above, we have conducted simulations (not shown here) in sediment transport regimes including both suspended load and bed-load transport, and it was observed that the convective terms in the bed-load transport were indeed able to eliminate the artificial roughness features. However, since the spurious roughness features do not negatively influence other element of the dune migration simulations in any way, we do not introduce artificial diffusion or other terms to smooth them out.

4.2.3 Statistics of Individual Particle Motions

The ability to simulate particle trajectories and represent particle composition statistics is one of the advantages of the Eulerian–Lagrangian framework. Therefore, this subsection is devoted to the study of these particle quantities. Figure 16(a) shows a scatter plot of particles at a time instance when the bed profile and the flow achieves approximate equilibrium. Each dot in the scatter plot indicates a parcel (a computational particle) as explained in Section 2.3.4, with the size indicating the number of physical particles they represent (ranging from 10 for the small ones to 20 for the large ones). That way, the particle concentration distribution in the channel can be inferred from the density and sizes of the parcels in the respective region. The concentration so obtained is displayed in Figure 16(b). Although the concentration field can also be obtained in the traditional methods (Kraft et al. 2011) by solving the convection–diffusion equation, the Eulerian–Lagrangian framework provides a better approach in that it avoids the ad hoc relations in the modeling of sediment deposition and diffusion, which are required in the traditional Eulerian approach.

It can be seen from Figure 16(a) that some parcels in the centerline represent more particles. In the simulations, a fixed number of parcels are released at each fixed time step regardless of the amount of physical sediment eroded during the period. As a result, the number of physical particles represented by each parcel is larger when the rate of erosion is larger. The erosion rate is larger during the initial period of the simulation when the bed profile is far from equilibrium, and gradually decreases as the dune profile approaches equilibrium. Hence, the parcels created in the initial period of the simulation represent more physical particles, and are more likely to be located near the channel center.

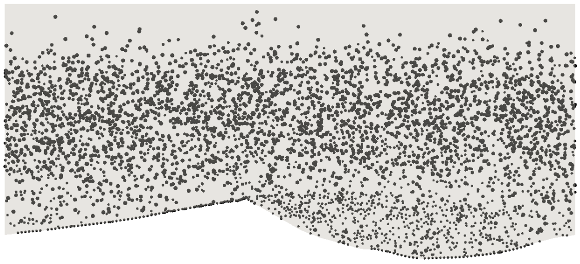

(a) Particle scatter plot

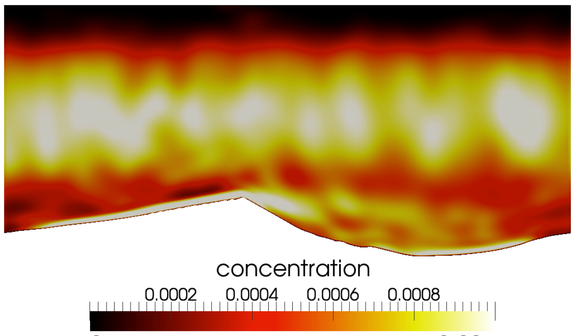

(b) Particle concentration

Figure 16 The distribution of sediment particles as indicated by (a) parcels (i.e., computational particles) in the channel and (b) particle concentration (i.e., volume fraction). Each parcel shown in panel (a) represents a number of physical particles range from 10 to 20. The sizes of the dots indicate the number of physical particles they represent, with larger dots representing larger numbers. In panel (b), the distribution of particle concentration in the channel is indicated by colors (grey levels).

Furthermore, from the particle distribution plot in Figure 16(a) one can distinguish three groups of particles according to their clustering behavior: (1) particles that are located in the boundary layer immediately (i.e. a few particle diameters) above the seabed; (2) particles that are concentrated in the recirculation region, particularly downstream of the dune crest; and (3) particles that are clustered near the channel center. The particles immediate above the seabed are mostly those fail to escape to the boundary layer during the injection process. Due to the small mean flow velocities and turbulent fluctuations in the boundary layer, the immersed gravity dominates other forces, i.e., drag, lift, and turbulent dispersion. Consequently, these particles will likely be short-lived as they will settle and deposit soon after being created under gravity. Another group of particles are those that are trapped in the reverse flow region on the leeward side of the dune. The recirculating flow pattern in this region is illustrated by the circular streamlines in Figure 17.

Although a small number of these particles eventually escape to the free stream region (above the dune crest level) due to the turbulent fluctuations, most will follow the mean flow velocities in the streamwise direction, and will stay trapped in this region. The gravity causes gradual deposition of these particles. On the other hand, in the reverse flow region the erosion flux is relatively small due to the small magnitude of the shear stresses (see Figure 13). This imbalance in the sediment budge leads to sand accretion on the leeward side of the dune, which, together with the erosion-dominated physics on the windward side of the dune, results in gradual migration of the sand dune. The particle distribution near the centerline is a result of balance between downward gravity settling and upward particle motion due to turbulent dispersion (see Eq. (16)) and the lift forces generated by mean velocity gradient (see Eq. (15)). Therefore, compared with the boundary layer and the recirculation zone, the channel center is a region where particles with longer residence time are more likely to be located. This is confirmed by the residence time distribution presented in Figure 18. Residence time can help distinguish different form of sediment transport (e.g., suspended load versus bed load). If the residence time of a particle is short, it may indicate the bed load is the dominant part of sediment transport; similarly, if the residence time is long, the suspended load is the dominant part.

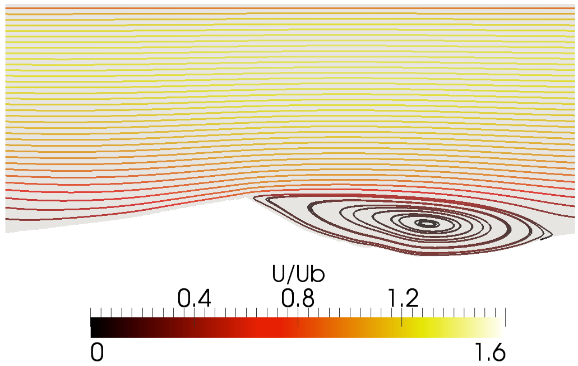

Figure 17 Streamline plot of the flow field, highlighting the recirculation region in the leeward side of the sand dune.

The residence times of individual particles are presented in Figure 18(a). It demonstrates that the particles near the sand bed boundary and on the leeward side of the dune have smaller residence time. Particles in these regions have been created recently and have not yet been suspended. The particles near the centreline of the channel have larger residence time since they are in dynamic equilibrium with gravity settling and upward suspension due to turbulent suspension, as pointed out above. Figure 18(b) displays the distribution of residence time for different particles in histogram. It can bee seen from Figure 18(b) that a significant portion of the particles have small residence time (less than $7L/U$). These are the group of particles identified in Figure 16(a) that are not able to escape from the boundary layer into the free stream. The histogram in Figure 18(b) also suggests a bimodal distribution of residence time, i.e., a particle tends to have either a very small residence time (near zero) or a very long residence time (near $t_r U_b/L = 120$.) The physical interpretation is that once a particle is suspended and successfully enter the free stream, it will likely stay there for a long time. Those that are not able to escape the boundary layer will deposit shortly after being created. Finally, we note that after the approximate equilibrium is achieved the number of particles suspended in the fluid flow is at different times are almost constant with very minor temporal fluctuations.

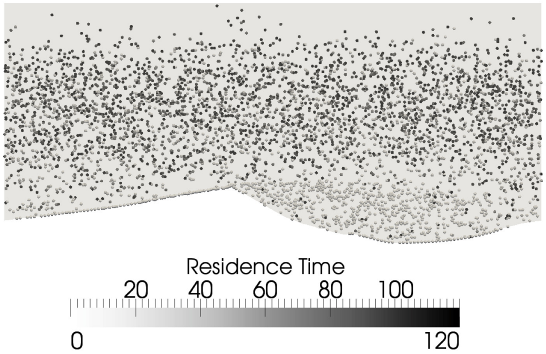

(a) Residence time of individual particles

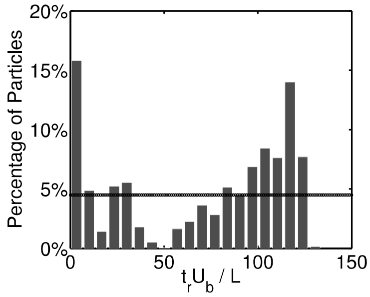

(b) Histogram of residence time distribution

Figure 18 The residence time of particles in the fluid flow, showing (a) the normalized residence time ($t_r U_b / L$) of particles at different locations in the channel, and (b) histogram of residence time of the particles.

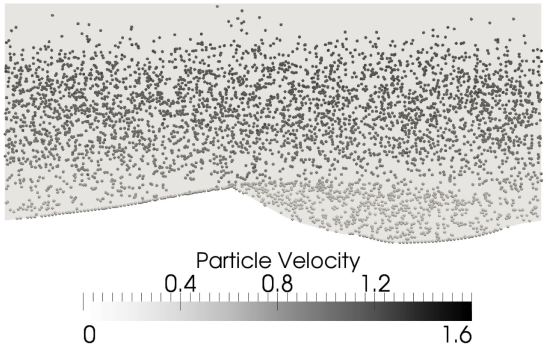

(a) Velocity of individual particles

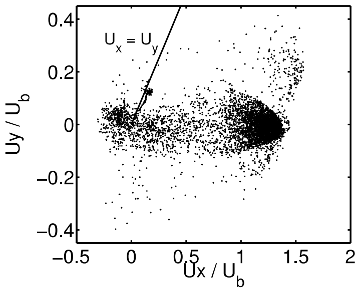

(b) Velocity distribution

Figure 19 A snapshot of particles velocity and distribution in the flow field, showing (a) the magnitude of particle velocity (normalized by U_b) at different locations in the channel, and (b) the scatter phase plot of horizontal and vertical components U_x/U_b, U_y/U_b, respectively, of the particle velocities. The straight line in panel (b) indicates $U_x = U_y$ on the phase plot.

The velocities of individual particles in the system are shown in Figure 19. Generally, the velocity of particles near the seabed boundary and on the leeward side is smaller than those near the centerline of the channel, as is evident from Figure 16. As the flow is in approximate equilibrium at the time instance shown here, the particle velocities shown in this plot represents to a large extent the velocity of the surrounding fluids, with the main difference being a relatively small sedimentation velocity of the particles in the vertical direction. The scattered phase plot for the horizontal and vertical components, U_x and U_y, of the particle velocities is shown in Figure 19(b). It can be seen that the velocity distribution of the particles is almost symmetric with respect to $U_y = 0$, and it is not biased in the downward direction, suggesting the sedimentation velocity to be rather small. This is expected since the mean flow is horizontal in most part of the domain (except for the recirculation region), and the vertical velocity of particles are mostly due to turbulent fluctuations reconstructed from the turbulent dispersion model, which are symmetric with respect to $U_y = 0$.

Most of the particles in the computational domain have horizontal velocities equal or slightly larger than the volume-averaged velocity U_b, as can be seen from the clustering in the phase plot near the point (U_x/U_b, U_y/U_b) = (1.2, 0) in Figure 19(b). Note that U_b is the velocity averaged over the entire volume. Considering the fact that there is a flow reversal region leeward of the dune with a negative horizontal velocity and that the velocities near the boundaries are smaller, the velocity near the channel center could be larger than U_b. The particles near the seabed or on the leeward side have smaller velocities, and they are indicated by the clustered dots near (U_x/U_b, U_y/U_b) = (0, 0) in Figure 19(b). Recalling from Section 2.3.2 that the particles are initialized with equal horizontal and vertical components, the particles around the oblique line $U_x = U_y$ in Figure 19(b) are mostly the newly created particles due to the erosion.

5. CONCLUSIONS

In this work, we developed an Eulerian–Lagrangian framework for the modeling of sediment transport and coastal dune migration. The fluid flow and the morphological evolution of the sediment bed are modeled in an Eulerian frame by solving the Reynolds-averaged Navier–Stokes equations and morphological equation, respectively, while the transport and dispersion of suspended particles are tracked in a Lagrangian frame by integrating the Newton's second law. As the developed framework is intended for applications where the flow is only dilutely loaded with sediments, the mass and momentum equations of the fluid flows are not modified due to the presence of particles; in other words, the fluid–particle interactions are only one-way coupled. However, the sediment erosion and deposition lead to morphological evolution, which in turn changes the computational domain and the mesh for the fluid flow solver, and this would cause changes on the flow field. Therefore, overall the flow solver and the particle tracking have a two-way coupling, albeit in an indirect way.

To represent physics that are not resolved in the numerical framework, empirical models are used for the sediment erosion flux, the drag and lift forces on particles, and the turbulent dispersion of suspended particles. Moreover, a model based on diffusion equation is proposed to account for the local sediment avalanches where repose angles are exceeded. This differential equation-based model has better computational efficiency compared with existing procedures in the literature, and is demonstrated to be able to represent the avalanche processes faithfully. It is noted that in the current framework no empirical model is needed to represent the deposition processes.

The developed framework is used to simulate the formation and development of sand dunes. The velocity profiles, the bed shear stresses, and particle statistics are analysed and compared with available benchmark results in the literature. Simulation results suggest that the proposed model is capable of representing many key phenomena in the sediment transport and dune migration processes. Further studies are needed to quantify the initialization procedure of particles in the flow field.

6. ACKNOWLEGEMENTS

We would like to acknowledge the support of Advanced Research Computing (ARC) of Virginia Tech for the computation resources. We appreciate the fruitful discussion with Jianxun Wang at Virgina Tech on the numerical simulations. The first author would be grateful for the technical advice of Yoshiyuki Sakai at Karlsruhe Institute of Technology for the development of the solver.

7. REFERENCES

Amsden, A. A., O'Rourke, P. J., and Butler, T. D. (1989) "KIVA-II: A computer program for chemically reactive flows with sprays." Technical report, Los Alamos National Lab., NM (USA).

Bakker, B., Struijk, A. J., and Nijdam, H. (1986) "Flume experiments on dunes under steady flow conditions (uniform sand, dm = 0.77 mm), description of bed forms." Technical report, WL–Delft Hydraul.

Best, J., and Kostaschuk, R. (2002) "An experimental study of turbulent flow over a low-angle dune." Journal of Geophysical Research: Oceans, 107(C9), pp18–1.

Bharadwaj, N., Rutland, C. J., and Chang, S. M. (2009) "Large eddy simulation modeling of spray-induced turbulence effects." International Journal of Engine Research, 10(2), pp97–119.

Chang, Y. S., and Scotti. A. (2003) "Entrainment and suspension of sediments into a turbulent flow over ripples." Journal of Turbulence, 4(019), pp1–22.

Chang, Y. S., and Scotti, A. (2004) "Modeling unsteady turbulent flows over ripples: Reynolds-averaged Navier–Stokes equations (RANS) versus large-eddy simulation (LES)." Journal of Geophysical Research, 109(C9), ppC09012.

Chanson, H. (2004) "Hydraulics of open channel flow." Butterworth-Heinemann.

Cherukat, P., Na, Y., Hanratty, T. J., and McLaughlin, J. B. (1998) "Direct numerical simulation of a fully developed turbulent flow over a wavy wall." Theoretical and computational fluid dynamics, 11(2), pp109–134.

Coleman, S. E., and Melville, B. W. (1994) "Bed-form development." Journal of hydraulic engineering, 120(5), pp544–560.

Crosato, A., Mosselman, E., Desta, F. B., and Uijttewaal, W. S. J. (2011) "Experimental and numerical evidence for intrinsic nonmigrating bars in alluvial channels." Water Resources Research, 47(3).

Escauriaza, C. and Sotiropoulos, F. (2011) "Lagrangian model of bed-load transport in turbulent junction flows." Journal of Fluid Mechanics, 666, pp36–76.

Farhat, C., Geuzaine, P., and Grandmont, C. (2001) "The discrete geometric conservation law and the nonlinear stability of ale schemes for the solution of flow problems on moving grids." Journal of Computational Physics, 174, pp669–694.

Fernandez Luque, R., and van Beek, R. (1976) "Erosion and transport of bed-load sediment." Journal of Hydraulic Research, 14(2), pp127–144.

Giri, S. and Shimizu, Y. (2006) "Numerical computation of sand dune migration with free surface flow." Water Resources Research, 42(10).

Haslinger, W. (1993) "Berechnung der turbulenten strmung in einem welligen, offenen gerinne mit hilfe eines mehrschichtenmodells." Master's thesis, Institut für Technische Thermodynamik, Technische Hochschule Darmstadt, Darmstadt, Germany.

Hudson, J. D., Dykhno, L., and Hanratty, T. J. (1996) "Turbulence production in flow over a wavy wall. Experiments in Fluids", 20(4), pp257–265.

Jacobsen, N. G. (2011) "A full hydro-and morphodynamic description of breaker bar development". ORBIT.

Jacobsen, N. G., Fredsøe, J., and Jensen, J. H. (2014) "Formation and development of a breaker bar under regular waves. Part 1: Model description and hydrodynamics." Coastal Engineering, 88, pp182–193.

Jasak, H., and Rusche, H. (2009) "Dynamic mesh handling in OpenFOAM." In Proceeding of the 47th Aerospace Sciences Meeting Including The New Horizons Forum and Aerospace Exposition, Orlando, Florida.

Jasak, H., and Tukovic, Z. (2006) "Automatic mesh motion for the unstructured finite volume method." Transactions of FAMENA, 30(2), pp1–20.

Knotek, S. and Jicha, M. (2014) "Modeling of shear stress and pressure acting on small-amplitude wavy surface in channels with turbulent flow". Applied Mathematical Modeling.

Kraft, S., Wang, Y., and Oberlack, M. (2011) "Large eddy simulation of sediment deformation in a turbulent flow by means of level-set method." Journal of Hydraulic Engineering, 137(11), pp1394–1405.

Luo, H., Baum, J.D., and Löhner, R. (2004) "On the computation of multi-material flows using ALE formulation." Journal of Computational Physics, 194, pp304–328.

Maaß, C., and Schumann, U. (1996) "Direct numerical simulation of separated turbulent flow over a wavy boundary." In Flow Simulation with High-Performance Computers II, pp227–241.

Madsen, O. S., and Grant, W. D. (1976) "Quantitative description of sediment transport by waves." Coastal Engineering Proceedings, 1(15).

Mierlo, M. C. L. M., and De Ruiter. J. C. C. (1988) "Turbulence measurements above artificial dunes." Report Q789, Delft Hydraulics Lab, Delft, The Netherlands.

Nabi, M., de Vriend, H. J., Mosselman, E., Sloff, C. J., and Shimizu, Y. (2013a) "Detailed simulation of morphodynamics: 2. sediment pick-up, transport and deposition." Water Resources Research.

Nabi, M., de Vriend, H. J., Mosselman, E., Sloff, C. J., and Shimizu, Y. (2013b) "Detailed simulation of morphodynamics: 3. ripples and dunes." Water Resources Research, 49(9), pp5930–5943.

Neill, S. P., Litt, E. J., Couch, S. J., and Davies, A. G. (2009) "The impact of tidal stream turbines on large-scale sediment dynamics." Renewable Energy, 34(12). pp2803–2812.

Nelson, J. M., and Smith, J. D. (1989) "Mechanics of flow over ripples and dunes." Journal of Geophysical Research: Oceans, 94(C6), pp8146–8162.

Niemann, S. L., Fredsøe, J., and Jacobsen, N. G. (2011) "Sand dunes in steady flow at low Froude numbers: Dune height evolution and flow resistance." Journal of Hydraulic Engineering, 137(1), pp5–14.

OpenCFD. (2013) "OpenFOAM: The Open Source CFD Toolbox."

O'Rourke, P. J. (1989) "Statistical properties and numerical implementation of a model for droplet dispersion in a turbulent gas." Journal of Computational Physics, 83(2), pp345–360.

Paola, C., and Voller, V. R. (2005) “A generalized Exner equation for sediment mass balance.” Journal of Geophysical Research: Earth Surface, 110, ppF04014.

Roulund, A., Sumer, B. M., Fredsøe, J., and Michelsen, J. (2005) “Numerical and experimental investigation of flow and scour around a circular pile.” Journal of Fluid Mechanics, 534, pp351– 401.

Saffman, P. G. (1965) “The lift on a small sphere in a slow shear flow. Journal of fluid mechanics, 22(02), pp385–400.

Stiesch. G. (2003) “Modeling engine spray and combustion processes.” Springer Berlin, 2003.

Thomas, P.D. and Lombard, C.K. (1979) “Geometric conservation law and its application to flow computations on moving grids.” AIAA Journal, 17, pp1030–1037.

Tukovic, Z., and Jasak, H. (2012) “A moving mesh finite volume interface tracking method for surface tension dominated interfacial fluid flow.” Computers & Fluids, 55, pp70–84.

van Rijn., L. C. (1984a) “Sediment pick-up functions.” Journal of Hydraulic Engineering, 110(10), pp1494–1502.

van Rijn., L. C. (1984b) “Sediment transport, part I: Bed load transport.” Journal of hydraulic engineering, 110(10), pp1431–1456.

Venditti, J. G., Church, M, and Bennett, S. J. (2005) “Morphodynamics of small-scale superimposed sand waves over migrating dune bed forms.” Water resources research, 41(10), ppW10423.

Wang, Z., and Larsen, P. (1994) “Turbulent structure of water and clay suspensions with bed load.” Journal of Hydraulic Engineering, 120(5), pp577–600.

Wilcox, D. C. (1998) “Turbulence modeling for CFD.” DCW Industries.

Willis, M., Masters, I., Thomas, S., Gallie, R., Loman, J., Cook, A., Ahmadian, R., Falconer, R., Lin, B., Gao, G., et al. (2010) “Tidal turbine deployment in the Bristol Channel: a case study.” Proceedings of the ICE-Energy, 163(3), pp93–105.

Yoon, H. S., El-Samni, O. A., Huynh, A. T., Chun, H. H., Kim, H. J., Pham, A. H., and Park, I. R. (2009) “Effect of wave amplitude on turbulent flow in a wavy channel by direct numerical simulation.” Ocean Engineering, 36(9), pp697–707.

Yoon, J. Y., and Patel, V. C. (1996) “Numerical model of turbulent flow over sand dune.” Journal of Hydraulic Engineering, 122(1), pp10–18.